

Jet trails and Mach cones: The interaction of microquasars with the ISM

Yoon, D.¹, Morsony, B.¹, Heinz, S.¹, Wiersema, K.², Fender, R.P.³, Russell, D.M.⁴, & Sunyaev, R.^{5,6}

ABSTRACT

A sub-set of microquasars exhibit high peculiar velocity with respect to the local standard of rest due to the kicks they receive when being born in supernovae. The interaction between the radio plasma released by microquasar jets from such high-velocity binaries with the ISM must lead to the production of trails and bow shocks similar to what is observed in narrow-angle tailed radio galaxies and pulsar wind nebulae. We present a set of numerical simulations of this interaction that illuminate the long term dynamical evolution and the observational properties of these microquasar bow shock nebulae and trails. We find that this interaction always produces a structure that consists of a bow shock, a trailing neck, and an expanding bubble. Using our simulations to model emission, we predict that the shock surrounding the bubble and the neck should be visible in H_α emission, the interior of the bubble should be visible in synchrotron radio emission, and only the bow shock is likely to be detectable in X-ray emission. We construct an analytic model for the evolution of the neck and bubble shape and compare this model with observations of X-ray binary SAX J1712.6-3739.

Subject headings: x-ray binaries, microquasars, jets

¹Department of Astronomy, University of Wisconsin-Madison, Madison, WI, USA

²University of Leicester, University Road, Leicester LE1 7RH, UK

³School of Physics & Astronomy, University of Southampton, Highfield, Southampton, S017 1BJ, UK

⁴Astronomical Institute Anton Pannekoek, University of Amsterdam, P.O. Box 94249, 1090 GE Amsterdam, the Netherlands

⁵Space Research Institute (IKI), Moscow, Russia

⁶Max-Planck-Institut für Astrophysik, Garching, Germany

1. Introduction

It is now well established that accretion onto black holes can lead to the production of powerful jets, both in the case of AGN, in which case we call the object a radio galaxy, and in the case of X-ray binaries (XRBs), in which case we call the object a microquasar. We have since learned that even neutron star X-ray binaries as well as some accreting white dwarfs behave in the same way (Fender et al. 2004; Migliari & Fender 2006; Tudose et al. 2009; Körding et al. 2008).

When powerful jets run into their environment, they produce bright external shocks (called hot spots or working surfaces) and generally inflate pockets of relativistic plasma that emit diffuse synchrotron emission. If the black hole is stationary, these pockets take on roughly ellipsoidal shapes and are called radio lobes or cocoons. They are surrounded by the interstellar or intergalactic gas that was occupying the volume prior to inflation, compressed into a narrow shell. This picture is most easily observed in the case of X-ray cavities in galaxy clusters inflated by AGN jets (Rafferty et al. 2006, and references therein), but has also been discovered around a few microquasars (Gallo et al. 2005; Hao & Zhang 2009).

However, when the black hole is moving at appreciable speed with respect to its environment, the ram pressure of the headwind can dramatically alter the dynamics of the outflowing radio plasma, sweeping it back and generating a bow shock ahead of the moving black hole. This has long been known in the case of radio galaxies (e.g. Miley et al. 1972), which, depending on the angle at which the plasma is bent back, are called narrow or wide angle tail sources (generically, these sources are also called “bent doubles”).

Given that the black holes at the core of microquasars are born in supernova explosions, and given that supernovae can impose significant kick velocities on the compact objects they produce, Heinz et al. (2008) suggested that a similar phenomenon to “bent doubles” should occur around a sub-population of microquasars: the high-velocity tail of the population of low-mass X-ray binaries (LMXBs). It is now known that several microquasars are moving through the ISM at relative velocities in excess of $v_{\text{ext}} > 100 \text{ km s}^{-1}$ (Mirabel et al. 2001).

The phenomenology of these trailed microquasars should be broadly similar to their supermassive AGN equivalent, leading to the production of a low-surface brightness trail of synchrotron emitting relativistic plasma, and a brighter bow shock nebula. While the mode of inflation is fundamentally different, the end product should also be very similar to pulsar wind bow-shock nebulae that are formed by interaction between strong wind from pulsars with significant kick velocities in the interstellar medium. The general bow shock features have been well observed in H_α emission for PSR B1957+20 (Stappers et al. 2003), PSR B0740-28 (Stappers et al. 2002), PSR J0437-4715 (Bell et al. 1995), and PSR B2224+65

(the “guitar” nebula) (Chatterjee & Cordes 2002). Also, G359.23-0.82 which is powered by PSR J1747-2958 shows bright head and X-ray & radio “trails” (Gaensler et al. 2004).

The first candidate of a bow shock around such a trailed source, the LMXB SAX J1712.6-3739, was discovered in an H_α image by Wiersema et al. (2009, originally found by van Zand et al. 1999). It is broadly consistent with the predictions of Heinz et al. (2008). Future searches for large scale nebula and diffuse synchrotron emission around known LMXBs are needed to further test the predicted existence of this population of sources.

The model developed in Heinz et al. (2008) was purely analytic and a number of important aspects of the evolution of such trailed microquasars was left open. Numerical simulations are needed to investigate the production of these sources in more detail and to confirm the qualitative predictions of Heinz et al. (2008).

In this paper, we model the evolution of the XRBs moving through the ISM by using 3-dimensional hydrodynamic simulations and to derive a more detailed dynamical model for the large scale evolution of these sources.

A key aim of this study is to develop quantitative diagnostics that can be used to derive important constraints on the core parameters of microquasars from observations of trailed microquasars, such as their age, their relative velocity with respect to the local standard of rest (v_{XRB}), and the jet power from observational parameters like the opening angle of the bow shocks, the size of the hot bubble at the terminus of the trail, and the brightness of the shock, trail, and bubble. In addition, our simulation results can be used to predict the brightness of H_α , bremsstrahlung, X-ray, and radio synchrotron emission and to design targeted observational searches for these sources.

This paper is organized as follows: In §2, we present the numerical method and the initial conditions for our numerical study. In §3, we discuss the evolution of XRBs, scaling relations, and observational expectations. In §4, we compare our results with new observations of the LMXB SAX J1712.6-3739. Finally, in §5 we summarize our results.

2. Technical Description

2.1. The code

Simulations are carried out in 3 dimensions with the FLASH 2.4 hydrodynamic code (Fryxell et al. 2000), which is a modular, adaptive mesh refinement code. It solves the Riemann problem using the piecewise-parabolic method. The code is formally accurate to second order. The gas is modeled with either an adiabatic equation of state with index

$\gamma=5/3$ or with radiative line cooling. Radiative cooling from an optically thin plasma is implemented in FLASH adopting a piecewise-power law approximation that evaluates a plausible fit to $\Lambda(T)$ within the temperature range of $4.4 \times 10^3 < T < 10^8\text{K}$

2.2. The jet nozzle

In order to simulate the injection of collimated, supersonic jets into the grid, we employ a numerical “nozzle”, as first developed and described in (Heinz et al. 2006): An internal inflow boundary of cylindrical shape placed at the location of the XRB, injecting fluid with prescribed energy, mass, and momentum flux to match the parameters we chose for the jet.

For reasons of numerical stability, we impose a slow lateral outflow with low mass flux in order to avoid complete evacuation of zones immediately adjacent to the nozzle due to the large velocity divergence at the nozzle. The injection of energy and mass due to this correction is negligible.

We generally follow the prescription for jet injection used in previous simulations of AGN jets described in (Heinz et al. 2006), but keep the location of the XRB fixed in space, instead letting the external medium stream by at velocity $-v_{\text{ext}}$. Unlike our AGN simulations, we do not impose a random jitter on the jet axis in this case.

We chose to inject the jet at an internal Mach number of 10. While our adiabatic simulations are strictly scale free, we picked a set of fiducial dimensions for our box that lead to the following natural scaling: For computational feasibility, we chose a jet velocity of $v_{\text{jet}} = 3 \times 10^9 \text{ cm s}^{-1}$. The jet is turned on initially and continues to inject material for the entire length of the simulation.

The simulations were carried out with Adaptive Mesh Refinement in order to capture the large dynamic range required, ensuring that the nozzle is resolved with at least 8 cells across. For our fiducial scaling, the maximum resolution for the standard model is about 0.156 pc near the jet nozzle.

Based on the estimated power of the jet in Cyg X-1 from Gallo et al. (2005), the jet power in our simulation is set to a constant value of $W_{\text{jet}} = 10^{37} \text{ ergs s}^{-1}$ in our fiducial scaling. Note that since the Cyg X-1 is known to be one of the most powerful XRB sources, sustaining the hard X-ray state for about 90% of the time. The jets in our model might be more powerful than those of typical LMXBs. However, with the exception of our simulations with cooling, our simulations are scale free and can thus be adjusted easily to other parameter combinations.

2.3. Initial conditions

We placed the XRB in a moving medium inside a box large enough that boundary conditions never influence the dynamics. We varied the velocity of the gas relative to the XRB to be $v_{\text{XRB}} = 30 \text{ km s}^{-1}$, 100 km s^{-1} and 300 km s^{-1} (see Table 1). The lowest velocity case represents a typical LMXB, given that the LMXB velocity dispersion is 37 km s^{-1} , while the largest represents the most extreme case plausible (a marginally unbound source). The simulations we ran for this study are listed in Tab. 1.

The fiducial ISM pressure we use is $P_0 = 3 \times 10^{-12} \text{ ergs cm}^{-3}$ following Cox (2005), and we use an ISM number density of $n_{\text{ISM}} = 1 \text{ cm}^{-3}$, giving a sound speed in the ISM of $c_s = 17.3 \text{ km s}^{-1}$.

Typically, simulations were carried out to 1 Myr in our fiducial scaling (much longer than the dynamical evolution of the jet, and long enough for the quasi-steady state of the bow shock and the self-similar solution we will discuss below to be established).

Table 1 also includes one case with our standard parameters and radiative cooling (with $v_{\text{XRB}} = 300 \text{ km s}^{-1}$), the hvc case. We used this run to verify that the morphology of our simulations are not strongly affected by cooling and to properly model emission (see §3.3). A further 3 simulations with cooling, fit1, fit2 and fit3, were carried out to attempt to match H_α observations of SAX J1712.6-3739 (see §4.1)

Because of the self-similar nature of the flow, the simulations lend themselves to a staggered refinement scheme. As we will describe below, the radio plasma forms of a large scale bubble and a neck connecting the XRB to this bubble. We can therefore de-refine the simulation on cylinders on increasing radius around the axis of propagation of the XRB and again de-refine with increasing distance from the XRB along the axis of propagation. We decrease the refinement by a factor of two for every power of two increase in radius and distance.

Table 1. Parameter of the simulations

Name	v_{XRB}	Maximum Resolution	Luminosity	Radiative Cooling
lv	30 km s^{-1}	0.312 pc	10^{37} erg/s	no
mv	100 km s^{-1}	0.156 pc	10^{37} erg/s	no
hv	300 km s^{-1}	0.156 pc	10^{37} erg/s	no
hvc	300 km s^{-1}	0.156 pc	10^{37} erg/s	yes
fit1	100 km s^{-1}	0.039 pc	$8.47 \times 10^{33} \text{ erg/s}$	yes
fit2	200 km s^{-1}	0.039 pc	$8.47 \times 10^{33} \text{ erg/s}$	yes
fit3	300 km s^{-1}	0.039 pc	$2.29 \times 10^{35} \text{ erg/s}$	yes

3. Results

3.1. Morphological Evolution

Heinz et al. (2008) presented a simple, analytic model for the long term dynamical evolution of trailed microquasars. Our simulations allow us to move beyond the initial heuristic model and describe the dynamics of microquasar driven bow shock nebulae in detail.

The initial evolution of the system follows the prediction of Heinz et al. (2008) almost exactly: The jets inflate a single large, roughly spherical bubble that expands following the self-similar solution for a continuously driven bubble by Castor et al. (1975), surrounded by a thin shell of swept-up ISM.

Initially, the expansion velocity of the bubble is much faster than the space velocity of the XRB, v_{XRB} , implying that the XRB remains roughly at the bubble’s center. As the expansion slows down, the XRB begins moving towards the shell and eventually breaks out of the expanding bubble.

At this point, the dynamic pressure of the ISM due to the XRB’s velocity causes the jets to bend backwards, and a trail of radio plasma is created behind the XRB, connecting it to the bubble. The radio plasma released by the XRB continues to inflate the bubble, akin to a balloon inflated by a straw. The bubble, therefore, continues to expand spherically even though the binary can be far outside the bubble.

As it propagates, the XRB is driving a bow shock into the ISM. As predicted in Heinz et al. (2008), dynamical instabilities develop at the contact discontinuity between the bow shocked ISM and the backflow along the radio trail, dissipating some of the backflow energy along the channel.

The dynamical evolution described above is shown in Fig. 1 as a time sequence of density slices through the center of the simulation box. Relativistic, axisymmetric simulations of a pulsar wind nebula in Bernstein & Hughes (2009) created a similar structure with a bow shock connected to an expanding bubble. This indicates that, away from the jet or wind source, the evolution of XRBs and pulsar nebulae are nearly identical, except for the scale.

3.2. Scaling relations

Based on the observed evolution of the trail and bubble, we can construct a simple analytic model for the inflation of bow shock nebulae by microquasars (and, by extension,

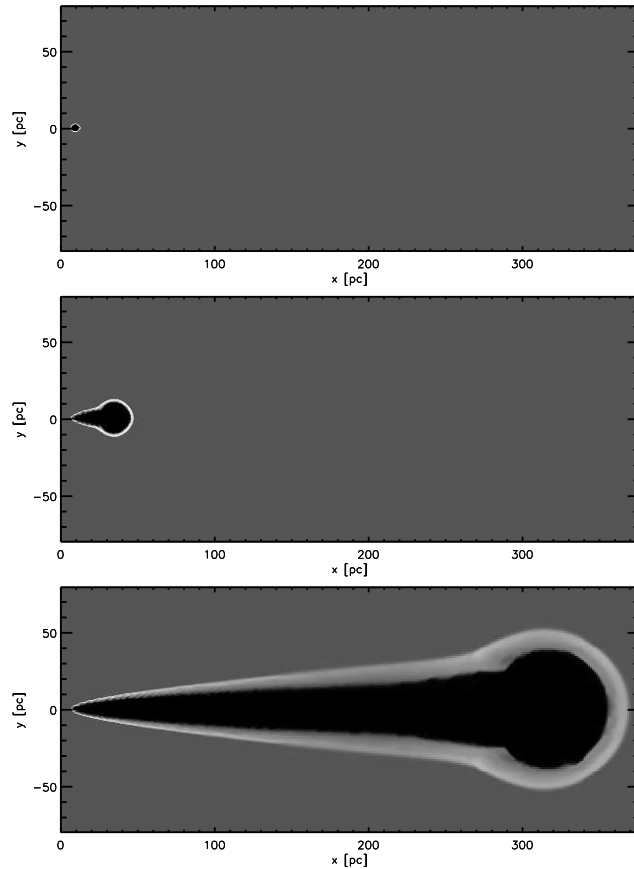


Fig. 1.— Density slice through our 300 km s^{-1} simulation at 10,000 years (top), 100,000 years (middle) and 1 Myr (bottom). The XRB is located toward the left of the images. At 10,000 years (top) the XRB is surrounded by a spherical bubble, although the XRB is nearing the left edge. At 100,000 years (middle), the XRB has broken out of the bubble and created a distinctive shape. The jets, directed up and down, are curved back at the bow shock (curved shock at left) and directed back to the large bubble to the right, where they terminate and power the bubble expansion. A neck connects the binary and bubble, and is surrounded by an oblique shock. At 1 Myr (bottom), the *shape* is similar to that at 100,000 years, except that the neck is more elongated, with a smaller opening angle.

pulsar wind bow shock nebulae) that can be tested directly against the simulations. This will allow us to formulate analytic expressions for observables.

The jets initially inflate a nearly spherical cavity that evolves as a wind driven bubble (Castor et al. 1975). The bubble expands as

$$R_b(t) = C_1^{1/5} \left(\frac{L}{\rho_0} \right)^{1/5} t^{3/5} \quad (1)$$

where L is the source luminosity, ρ_0 is the ISM density and C_1 is a constant that equals $\frac{25}{14\pi}$ for an adiabatic index of $\Gamma = 5/3$. In terms of the fiducial parameters for our simulations, this is

$$R_b(t) = 13.1 \text{ parsec} \left(\frac{L_{37}}{\rho_{0H}} \right)^{1/5} t_5^{3/5} \quad (2)$$

where $L_{37} = \frac{L}{10^{37} \text{ erg s}^{-1}}$, $\rho_{0H} = \frac{\rho_0}{1.67 \times 10^{-24} \text{ g cm}^{-3}}$, and $t_5 = \frac{t}{100,000 \text{ years}}$. The expansion velocity of the bubble is

$$v_b(t) = \frac{3}{5} C_1^{1/5} \left(\frac{L}{\rho_0} \right)^{1/5} t^{-2/5} = 76.7 \text{ km s}^{-1} \left(\frac{L_{37}}{\rho_{0H}} \right)^{1/5} t_5^{-2/5} \quad (3)$$

and the pressure inside the bubble is

$$P_b(t) = P_0 \left(\frac{5}{4} M_b^2 - \frac{1}{4} \right) \quad (4)$$

where $M_b = \frac{v_b}{\sqrt{\gamma P_0 / \rho_0}}$ is the Mach number of the spherical shock and P_0 is the ISM pressure. Assuming at least a moderately strong shock, the pressure goes to

$$P_b(t) \approx \frac{5}{4} P_0 M_b^2 \approx \frac{27}{100} C_1^{2/5} L^{2/5} \rho_0^{3/5} t^{-4/5} \approx 8.25 \times 10^{-11} \text{ erg cm}^{-3} L_{37}^{2/5} \rho_{0H}^{3/5} t_5^{-4/5} \quad (5)$$

Initially, the expansion of this bubble is faster than the velocity of the XRB. However, as the expansion of the bubble slows while the velocity of the source remains constant, the source eventually breaks out of the bubble at a time t_{break} . The breakout time scales with source velocity v_s as

$$\begin{aligned} t_{\text{break}} &= C_1^{1/2} \left(\frac{L}{\rho_0} \right)^{1/2} v_s^{-5/2} \\ &= 185,000 \text{ years} \left(\frac{L_{37}}{\rho_{0H}} \right)^{1/2} \left(\frac{v_s}{100 \text{ km s}^{-1}} \right)^{-5/2} \end{aligned} \quad (6)$$

The radius of the bubble at the breakout time therefore scales as

$$R_{break} = C_1^{1/5} \left(\frac{L}{\rho_0} \right)^{1/5} t_{break}^{3/5} = C_1^{1/2} \left(\frac{L}{\rho_0} \right)^{1/2} v_s^{-3/2} = 18.9 \text{ parsec} \left(\frac{L_{37}}{\rho_{0H}} \right)^{1/2} \left(\frac{v_s}{100 \text{ km s}^{-1}} \right)^{-3/2} \quad (7)$$

After breakout, the source continues to power bubble expansion. A bow shock develops in front of the source which bends the jets back in the opposite direction of the source motion. A low-density channel remains which connects the source to the bubble. Jet material flows back through this channel, adding energy to the interior of the expanding bubble. So long as the volume of this channel remains small compared to the volume of the bubble, the expansion rate of the bubble continues to be described by eqn. 1, the self-similar equation of a continuously powered bubble.

As seen in Fig. 1, the resulting shape is an expanding spherical bubble connected to the source by a thin neck. The neck consists of a shock surrounding a narrow cavity filled with jet material. At any point x along the neck, the shape is described by w_1 , the width of the inner cavity, and w_2 , the distance from the mid plane to the outer edge of the shock. In the frame of the binary, the cavity has a fixed shape and is in pressure balance with the surrounding shocked material. The flow of material can therefore be described using an adiabatic equation of state, the Bernoulli equation and mass continuity:

$$P_x = a\rho_x^\gamma \quad (8)$$

$$\frac{1}{2}v_x^2 + \frac{\gamma}{(\gamma - 1)} \frac{P_x}{\rho_x} = b \quad (9)$$

$$\rho_x v_x w_1^2 = c \quad (10)$$

where v_x , ρ_x and P_x are the velocity, density and pressure of material in the cavity at position x , γ , the adiabatic index, is $5/3$, and a , b and c are constants. In term of a , and with $\gamma = 5/3$, $b = a^{3/5}(\rho_0 v_s^2)^{2/5}$ and $c = L a^{-3/5}(\rho_0 v_s^2)^{-2/5}$.

Rearranging eqns. 8 to 10 we solve for w_1 and find that

$$w_1 = \left(\frac{ca^{3/5}}{\sqrt{2a^{3/5}}} \right) \frac{1}{\left[(\rho_0 v_s^2)^{2/5} P_x^{6/5} - \frac{5}{2} P_x^{8/5} \right]^{1/4}} \quad (11)$$

Making the approximation $P_x \ll \rho_0 v_s^2$ (i.e., the source velocity is supersonic), this reduces to

$$w_1 = 5^{-1/4} 2^{1/2} L^{1/2} a^{3/10} (\rho_0 v_s^2)^{-3/10} P_x^{-3/10} = C_2 P_x^{-3/10} \quad (12)$$

The pressure will be set by the jump conditions for an oblique shock, with θ and β the angle with respect to the direction of motion of the inner and outer edges of the shock, respectively:

$$\tan(\theta) = \frac{M_0^2 \sin^2 \beta - 1}{\tan \beta (1 + \frac{\gamma+1}{2} M_0^2 - M_0^2 \sin^2 \beta)} \quad (13)$$

$$\frac{P_x}{P_0} = \frac{2\gamma M_0^2 \sin^2 \beta - (\gamma - 1)}{(\gamma + 1)} \quad (14)$$

where $M_0 = v_s / \sqrt{\gamma P_0 / \rho_0}$ is the Mach number of the binary relative to the ISM, $\tan \theta = dw_1/dx$ and $\tan \beta = dw_2/dx$. Making the approximation that θ and β are small, this reduces to

$$\theta = \frac{M_0^2 \beta^2 - 1}{\frac{4}{3} \beta M_0^2} \quad (15)$$

$$P_x = P_0 \left(\frac{5}{4} M_0^2 \beta^2 - \frac{1}{4} \right) \quad (16)$$

$$\beta = \sqrt{\frac{4 \frac{(w_1/C_2)^{-10/3}}{P_0} + 1}{5 M_0^2}} \quad (17)$$

Substituting we find

$$\theta = \frac{dw_1}{dx} = \frac{3(C_2^{10/3} - P_0 w_1^{10/3})}{M_0 P_0 w_1^{10/3}} \left(\frac{20 C_2^{10/3}}{P_0 w_1^{10/3}} + 5 \right)^{1/2} \quad (18)$$

This differential equation can then be integrated numerically to find $w_1(x)$ and this in turn can be used to find $w_2(x)$.

As the pressure drops along the neck, however, it eventually reaches a minimum value equal to the pressure in the expanding bubble. Beyond this point, the angle of the shock

is constant such that the post-shock pressure is equal to the P_b , the pressure in the bubble, which is set by the expansion rate of the bubble v_b . The incoming velocity towards the shock will be $v_s - v_b$, because the bubble is expanding towards the source, giving a minimum shock angle of

$$\beta = \frac{v_b}{v_s - v_b} = \frac{dw_2}{dx} \quad (19)$$

The angle of the inner surface is then approximately

$$\theta = \frac{M_2^2 \beta^2 - 1}{\frac{4}{3} M_2^2 \beta} = \frac{dw_1}{dx} \quad (20)$$

where $M_2 = (v_s - v_b)/\sqrt{\gamma P_0/\rho_0}$ is the Mach number of the shock. In our simulations, this asymptotic limit dominates and the shape described by eqn. 18 only describes a small region near the jet source. Note that the width of the neck where it reaches the minimum value of β is described by eqn. 12 with $P_x = P_b$, giving $w_1(P_b) = C_2 P_b^{-3/10}$. This equation depends on the normalization constant a in the adiabatic equation (eqn. 8), which in practice depends on the amount of mixing between jet and ISM material. The width at this point also depends on the radius of curvature of the bow shock, which is not taken into account in this analytic model. Therefore, we use a as a free parameter to get the proper fit for the width of the neck where the minimum value of β is reached.

Figure 2 shows density slices of the 300 km s⁻¹, 100 km s⁻¹ and 30 km s⁻¹ simulations (models hv, mv and lv) at 1 Myr. The white lines are results of our analytic model for the bubble size, $w_1(x)$ and $w_2(x)$. In the first two cases, the predicted shape of the inner and outer edge of the neck are a good fit to the simulations. In the 30 km s⁻¹ case, the XRB is still inside the spherical bubble at 1 Myr.

The outer shock angle β decreases with time as the pressure in the bubble and the expansion velocity drop. The width of the neck where it meets the bubble is approximately

$$w_{2,meet} = \beta(v_s t - R_b) + w_1(P_b) \quad (21)$$

$$w_{2,meet} = \frac{v_b}{v_s - v_b} \left(v_s t - \frac{5}{3} v_b t \right) + C_2 \left(\frac{5}{4} P_0 M_b^2 \right)^{-3/10} \quad (22)$$

Asymptotically, this width goes to $w_{2,meet} = \beta v_s t = v_b t = \frac{3}{5} R_b$. Therefore, the ratio of

the bubble radius to the neck width approaches a constant ratio of $3/5$, and the width of the neck is always smaller than the radius of the bubble.

The volume of the neck scales asymptotically as

$$V_{\text{neck}} = \frac{1}{3}\pi v_s t \left(\frac{3}{5}R_b\right)^2 = \frac{1}{5}\pi C_1^{2/5} v_s \left(\frac{L}{\rho_0}\right)^{2/5} t^{11/5} = 3.23 \times 10^{58} \text{ cm}^3 \left(\frac{v_s}{100 \text{ km s}^{-1}}\right) \left(\frac{L_{37}}{\rho_{0H}}\right)^{2/5} t_5^{11/5} \quad (23)$$

while the volume of the bubble scales as

$$V_{\text{bub}} = \frac{4}{3}\pi R_b^3 = \frac{4}{3}\pi C_1^{3/5} \left(\frac{L}{\rho_0}\right)^{3/5} t^{9/5} = 2.75 \times 10^{59} \text{ cm}^3 \left(\frac{L_{37}}{\rho_{0H}}\right)^{3/5} t_5^{9/5} \quad (24)$$

the ratio of the volumes is therefore

$$\frac{V_{\text{neck}}}{V_{\text{bub}}} = \frac{9}{100} \frac{v_s t}{R_b} = \frac{3}{20} C_1^{-1/5} v_s \left(\frac{L}{\rho_0}\right)^{-1/5} t^{2/5} = 0.117 \left(\frac{v_s}{100 \text{ km s}^{-1}}\right) \left(\frac{L_{37}}{\rho_{0H}}\right)^{-1/5} t_5^{2/5} \quad (25)$$

The volume of the neck and bubble will eventually become equal when the length of the neck ($v_s t$) is about 11.1 times the bubble radius. The width of the shock where it meets the bubble is about $w_{2,\text{meet}} = \frac{3}{5}R_b$, so the angle when the volumes are equal is $\beta = 27/500 = 0.054$. However, the angle of the shock around the neck cannot be less than $\beta \simeq 1/M_0$, so the volumes become equal before the shock becomes weak only if $M_0 \geq 18.5$. Our assumption that the volume of the neck is small will hold until bubble expansion starts to become marginally sonic, unless the source has a very high Mach number relative to its surroundings.

While our simulations have not run long enough to probe the sub-sonic regime of bubble expansion, it is worth speculating about the late state evolution of trails and bubbles. Given that the bounding pressure of the bubble will be dominated by the internal pressure of the ISM, the expansion velocity of the bubble will drop below the self-similar value for an energy driven bubble (with $R \propto t^{1/3}$). In addition, the ISM will no longer be strongly compressed into a narrow shell. Since the neck and bow shock will maintain their stationary shape, one should expect that the late state evolution of a bow-shock/trail nebula will eventually lose the terminating bubble and the trail pressure will eventually approach the ISM pressure, consistent with the late state structure of the trail proposed in Heinz et al. (2008).

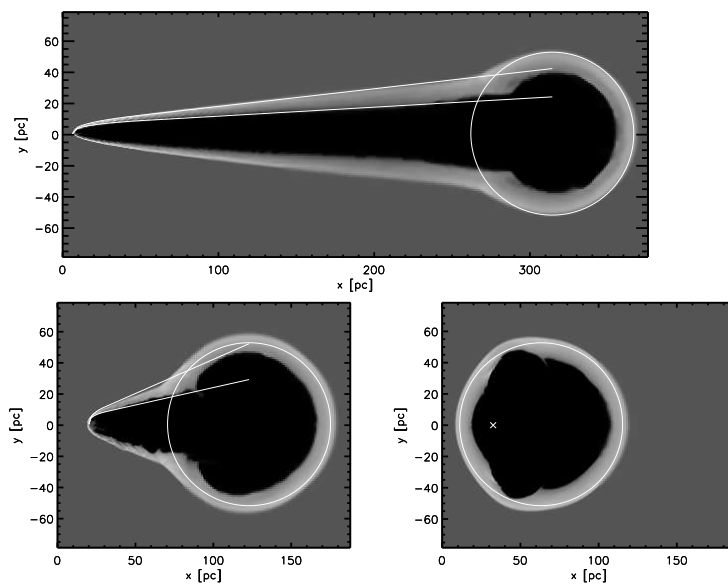


Fig. 2.— Density slice of 300 km s^{-1} (upper), 100 km s^{-1} (lower left) and 30 km s^{-1} (lower right) simulations at 1 Myr. The white curves trace the analytic solution for w_1 and w_2 , the neck shape, and the circle is the size of the bubble from eqn. 1. Values of a used to fit the bow shock width are 10^{31} for the 300 km s^{-1} simulations and 10^{33} for the 100 km s^{-1} simulation. In the 30 km s^{-1} simulation the XRB (marked with an \times) is still inside the bubble, but significantly offset from the center.

3.3. Observable properties of microquasar bow shock nebulae and trails

3.3.1. H_α emission

For XRBs moving supersonically through cold or warm ISM, the compressed, hot gas in the bow shock will produce collisionally excited line emission, most importantly H_α (as well as the classic spectrum of nebular lines like [OIII]). In fact, Wiersema et al. (2009) detected the nebula of SAX J1712.6-3739 in H_α . Our models support the jet-ISM interaction scenario (Heinz et al. 2008) and the numerical simulations show an apparent quantitative agreement with the observed results for H_α emission.

To calculate the H_α emission, we first determine the ionization balance in the shocked gas, using the MAPPINGS III code (Sutherland & Dopita 1993); the code uses a time-dependent algorithm for accurate equilibrium balance calculation. The typical temperature of the shocked shell is estimated to be around $10^5 - 10^6$ K in the adiabatic case, hence the gas is inferred to be nearly fully ionized at the shocked region. Figure 3 (bottom left panel) shows the surface brightness in H_α for the model hv. Note that all simulations can be scaled with XRB jet luminosity by reducing the predicted surface brightness, nebula size, and simulation time by a factor of $(L_{37})^{-1/2}$.

The bubble is relatively bright in H_α . The shock around the neck is also visible in H_α in fig. 3. A similar feature has been identified with SAX J1712.6-3739 (Wiersema et al. 2009). We discuss the morphological similarity between that source and our simulations in §4.1.

Radiative cooling has little influence on the dynamical evolution of the XRBs. The upper panels of fig. 3 reveal that overall morphologies for two models (with and without radiative cooling) are broadly similar. Radiative cooling leads to a significantly thinner shell of shocked material around the bubble and neck, giving the appearance of a slightly narrower neck. Because of the cooling-induced contraction of the gas, the shell also appears to develop some irregularities in shape, though the overall shape of the hot (radio) plasma inside the trail and bubble occupies essentially the same volume.

However, the radiative cooling has a pivotal role for H_α , because of the strong temperature sensitivity of the ionization balance and thus the recombination line emission. This is because the cooling time scale is comparable to the dynamical time scale of XRBs, leading to significantly lower temperatures in the shell than in a purely adiabatic simulations.

The bow shock immediately surrounding the XRB is very dim because the temperature is too high for strong H_α emission. As cooling becomes important down stream, the temperature at the shock quickly drops to the range of a few 10,000 K. As a result, the emission becomes stronger by about a factor of 50.

Because H_α emission depends non-trivially on temperature, it is not straight forward to express brightness predictions semi-analytically. Figure 3 is therefore specific to our simulation using fiducial parameters only.

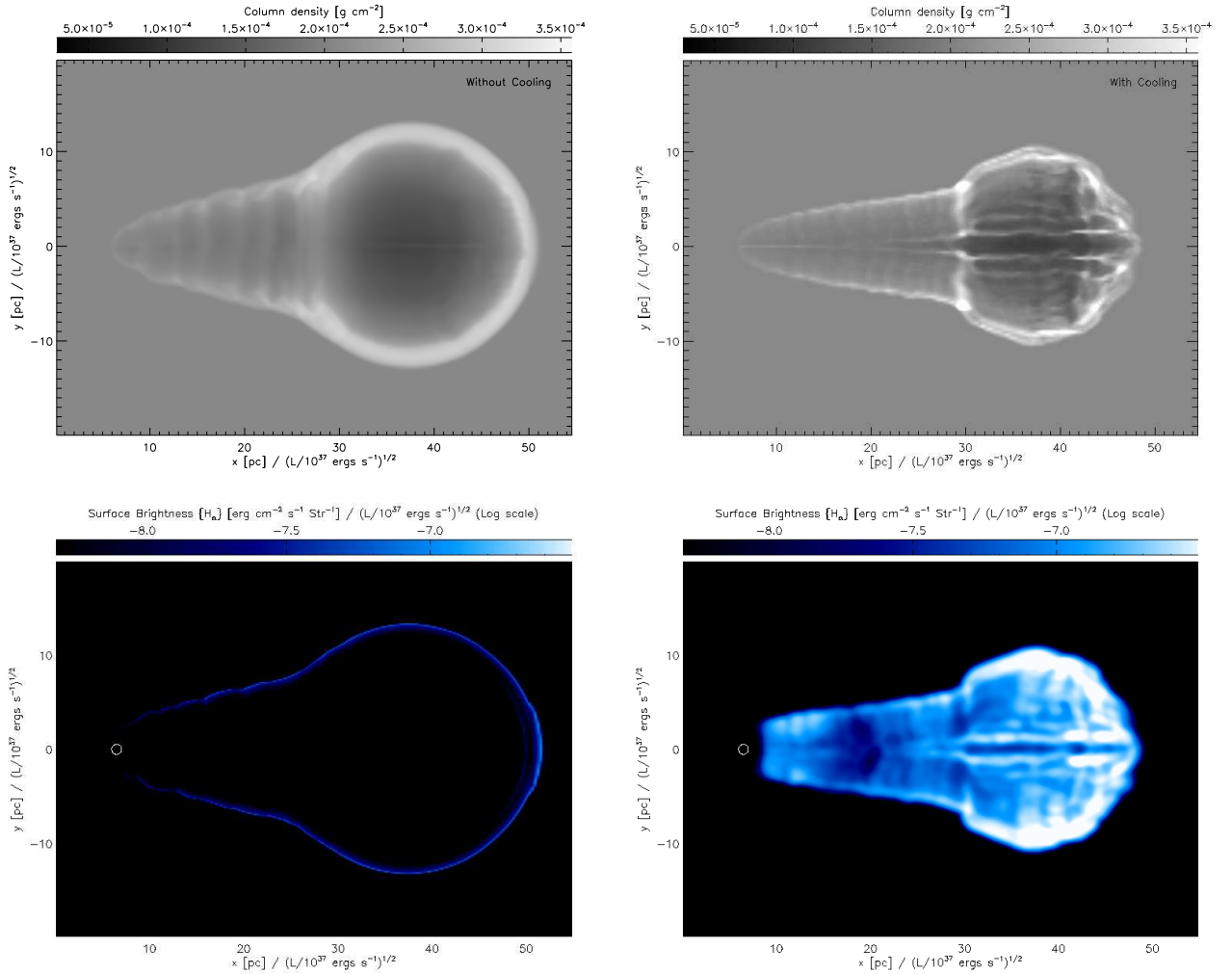


Fig. 3.— The density contour map for the model without the radiative cooling (upper left) and with the radiative cooling (upper right) at 100,000 yr ($v_{xrb} = 300 \text{ km s}^{-1}$). The bottom panels shows H_α emission for each case (log scale). The predicted surface brightness can be scaled to different XRB jet luminosities by reducing the surface brightness, size scale and simulation time by a factor of $L_{37}^{-1/2}$.

3.3.2. Radio emission

Given that the trail itself should be filled by magnetized, relativistic plasma released by the jets, they will emit synchrotron radiation. As the plasma travels along the jet, particles will cool both adiabatically and due to synchrotron losses. As is well known from studies of AGN jets and radio lobes, this introduces a cutoff to the electron energy distribution and to the synchrotron spectrum.

Following, e.g., Heinz & Begelman (1997), the cutoff frequency, as a function of travel time along the trail, will be given by

$$\gamma_{max} \simeq \frac{\left(\frac{P}{P_0}\right)^{1/4}}{\int \frac{4}{3}\sigma_T U_B \left(\frac{P}{P_0}\right)^{1/4} dt}. \quad (26)$$

with an associated cutoff frequency of

$$\nu_{max} \approx \frac{9eB\gamma_{max}^2}{4\pi m_e c^2}, \quad (27)$$

Given that the flow through the trail assumes a quasi-steady state behind the XRB, we can simply integrate this equation through single frames to lowest order to derive the cooling frequency as a function of position along the trail. The result is shown in fig. 4. For our fiducial parameters, the cooling frequency is estimated to fall within $10^{13} - 10^{15}$ Hz, well above the radio band.

This implies that synchrotron emission should be a good tracer of these trails at all frequencies, not just at low frequencies. This is in contrast to the estimates in Heinz et al. (2008), who suggested that cooling could be important along the trail. The reason for this difference is the significant backflow velocity along the trail, which was left as a free parameter in Heinz et al. (2008), and which allows radio emitting particles to traverse the trail without significant losses.

Figure 5 shows synchrotron surface brightness for the 300 km s^{-1} simulation at 100,000 years. Surface brightness for synchrotron emission is strongest at the front-edge where the jets are bent by ram pressure. The terminal radio bubble is also bright and emits the bulk of the total radio luminosity.

In fig. 5, the typical brightness temperature inside the bubble is estimated to be of order a few K in model hvc at 0.1 Myr at a frequency of 1 GHz. Since the synchrotron emission

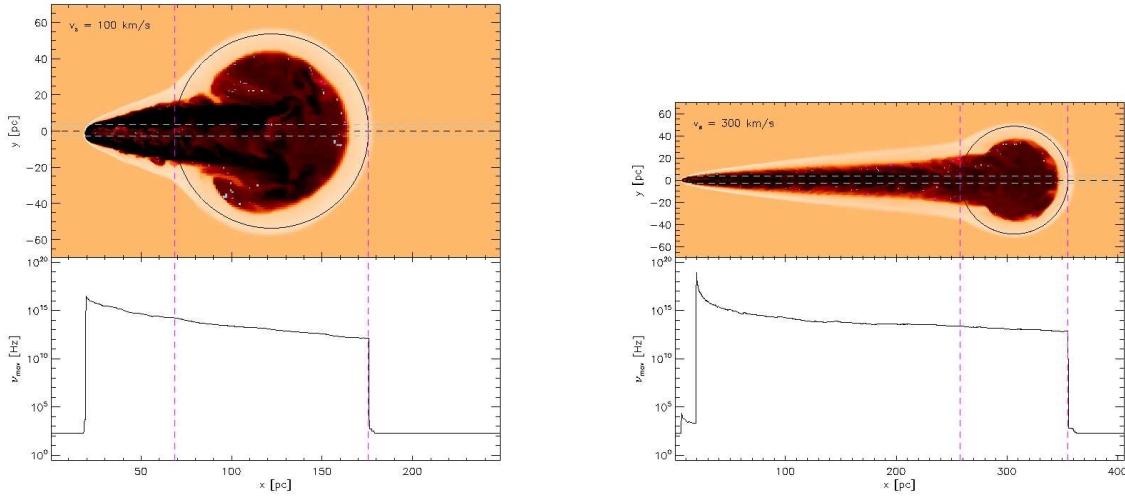


Fig. 4.— Synchrotron cooling frequency for X-ray binaries at 100 km s^{-1} (left panel) and 300 km s^{-1} (right panel) at 1 Myr. Top images indicate the density map with logarithmic scale. The vertical magenta lines indicate edges of the bubble area (marked with the solid circle). The cutoff frequency is calculated by integrating along the two blue lines and assuming a steady state.

depends only on the pressure, the typical values of brightness temperature in other models ($v_{\text{XRB}}=30, 100 \text{ km s}^{-1}$) are essentially the same.

If the intensity of synchrotron emission is high enough, synchrotron self-absorption will occur and the emission will drop out at low frequencies, proportional to $\nu^{5/2}$ regardless of the electron power index. However, in our particular simulation, the optical depth at 1 GHz is quite transparent (about $\tau = 10^{-2}$) so this effect would be negligible.

The bright temperature can be extrapolated into a few 10^{-3} K in submm wave bands that might be detectable by a new generation detectors such as SCUBA-2 or ALMA. In the case of the XRBs in our galaxy, assuming that the distance would be a few kpc, the angular size of the bubble is large enough to be resolved by these detectors.

Since the pressure inside the bubble decreases with time, the surface brightness will also decrease with time and synchrotron radiation will be easier to observe at an earlier XRB age if the bubble is resolved.

The synchrotron emission from the bubble can easily be predicted analytically. For a power-law distribution of electrons, $N(\gamma)d\gamma = A\gamma^{-p}d\gamma$: if we assume the power-law index (p) is 2.5, the total emissivity per unit volume per unit frequency can be calculated as,

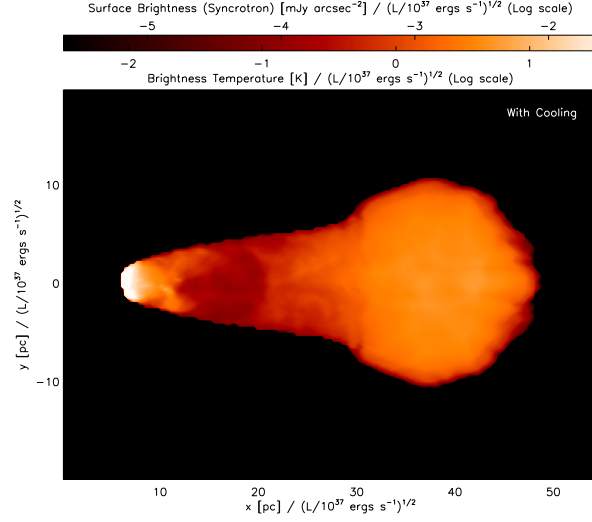


Fig. 5.— Surface brightness of radio synchrotron emission for the frequency of 1 GHz at 100,000yr ($v_{\text{XRB}} = 300 \text{ km s}^{-1}$).

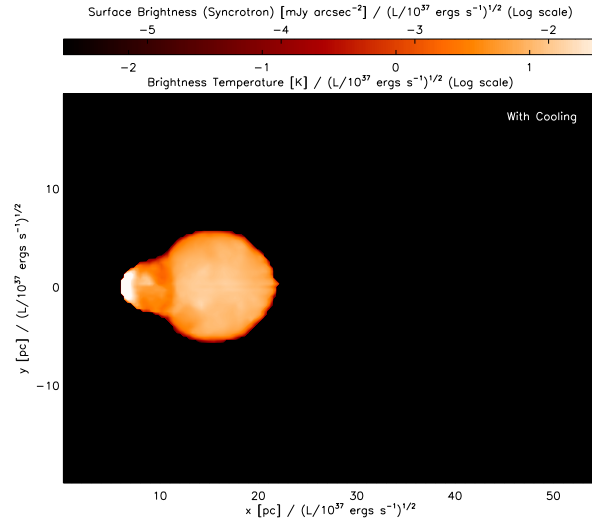


Fig. 6.— Surface brightness of radio synchrotron emission for the frequency of 1 GHz at 30,000yr ($v_{\text{XRB}} = 300 \text{ km s}^{-1}$).

$$\epsilon_{sync} = C_3 P^{15/8}, \quad (28)$$

where P is the pressure in the bubble and C_3 is approximately 1.44×10^{-17} and depends on the ratio of electron to magnetic pressure. Throughout this discussion we will assume that the plasma is in equipartition (with equal energy density in electrons and magnetic field), making the estimated fluxes *upper limits*.

The pressure of the hot bubble can be estimated from the shock jump conditions. If we set the adiabatic index to $5/3$, the pressure jump condition in the shell of the bubble are given by eqn. 5.

Figure 7 shows that the inferred post-shock pressure is consistent with the simulation results, although the data from the simulation have a slightly smaller values. The small discrepancy is negligible in estimating the surface brightness.

The surface brightness can be derived from the emissivity (eqn. 28) with post-shock pressure and the path length of the line of sight in bubble. Hence the maximum value of path length is $R_{bub}(t)$, and the surface brightness becomes

$$\begin{aligned} I_{sync} &\approx \frac{C_3}{4\pi} \left(\frac{27}{100} C_1^{2/5} L^{2/5} \rho_0^{3/5} t^{-4/5} \right)^{15/8} C_1^{1/5} L^{1/5} \rho_0^{-1/5} t^{3/5} \\ &\approx 1.37 \times 10^{-3} \text{mJy arcsec}^{-2} \times (L_{37})^{19/20} (\rho_{0H})^{37/40} \left(\frac{t}{1\text{Myr}} \right)^{-9/10} \end{aligned} \quad (29)$$

This theoretical calculation is in good agreement with numerical data shown in fig. 8. The relation confirms that the synchrotron emission decreases over time, implying that younger XRBs are more easily detected in the radio.

XRB bubbles in other galaxies will be difficult to resolve with radio observations, but may be detectable as unresolved sources, at locations *different* from the X-ray point source. If we set the distance to the XRBs to be D , then we can estimate the unresolved flux as,

$$\begin{aligned} \text{Flux}_{sync} &\approx \frac{C_3}{16\pi} \left(\frac{27}{100} C_1^{2/5} L^{2/5} \rho_0^{3/5} t^{-4/5} \right)^{15/8} C_1^{3/5} L^{3/5} \rho_0^{-3/5} t^{9/5} D^{-2} \\ &\approx 0.04 \text{ mJy} \times (L_{37})^{27/20} (\rho_{0H})^{21/40} \left(\frac{t}{1\text{Myr}} \right)^{3/10} \left(\frac{D}{1\text{Mpc}} \right)^{-2} \end{aligned} \quad (30)$$

This flux includes only the bubble area, and neglects the synchrotron emission from near the jets. Because we do not resolve the base of the inner regions of the jet in our simulations, and because microquasars are generally highly variable, we cannot make any quantitative statements about the relative flux from the inner jet and the bubble. Note that the total flux from the trail and bubble *increases* with time, indicating that older XRBs will be easier to detect than young ones in unresolved observations.

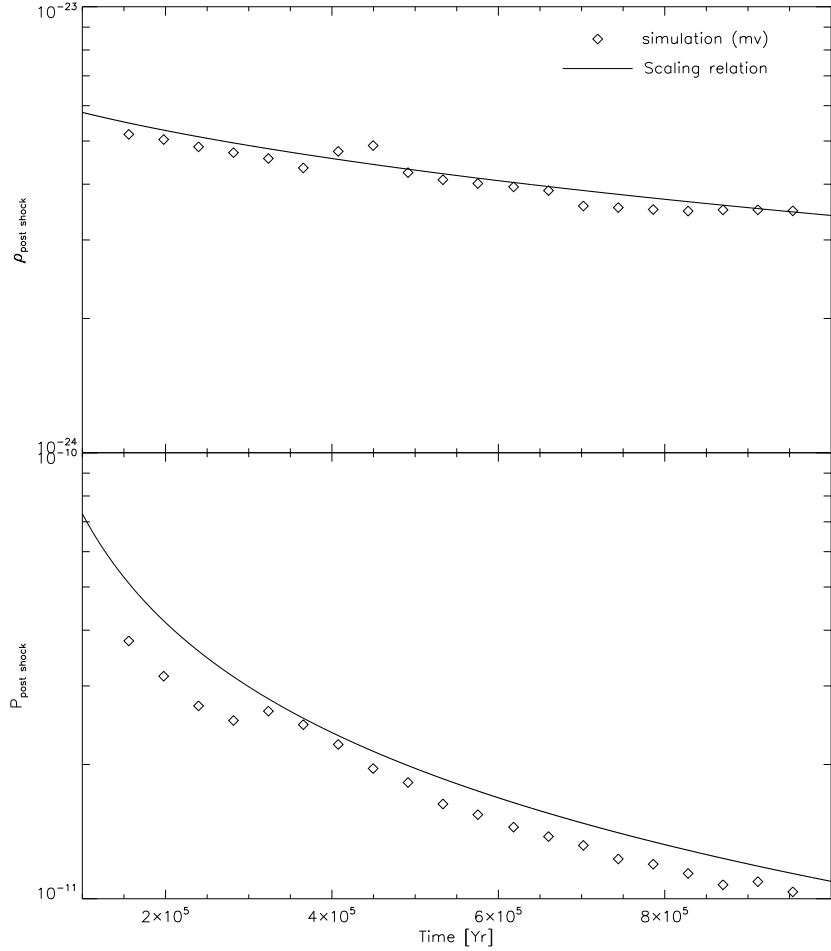


Fig. 7.— The solid line indicates that post shock pressure and density derived from scaling relation and diamond marks the results from simulation.

The state-of-the-art radio observatories are well suited for this type of objects; the eVLA has been upgraded to have the excellent sensitivity, frequency coverage, and imaging capability that allows for good quality radio spectra resolved over the source, and the WSRT APERTIF that has very large field of view at 1.4 GHz, allowing for deep continuum surveys capable of detecting trailed nebula.

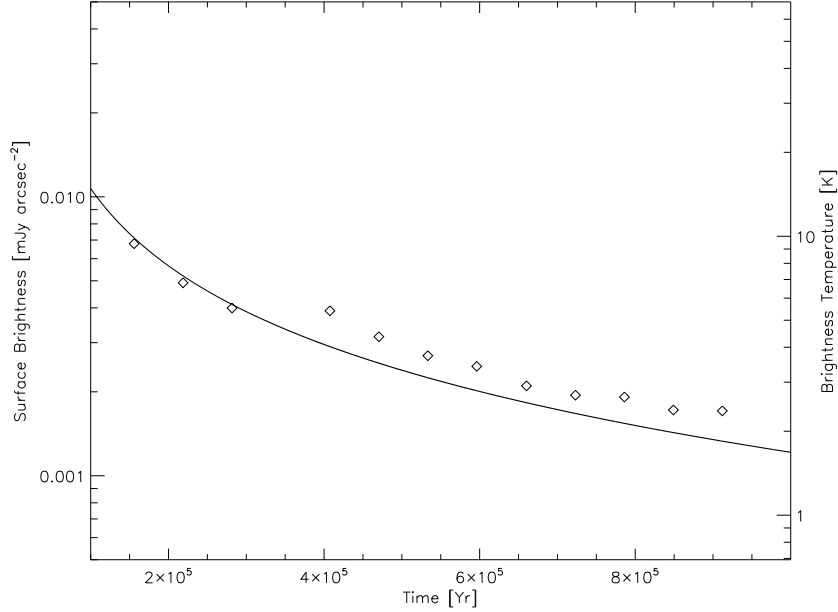


Fig. 8.— The solid line indicates the theoretically expected surface brightness in synchrotron emission and diamond indicates the results from simulation.

3.3.3. Free-free emission

For the expected temperature range in the bow shock, we can expect the gas to be mostly or completely ionized, which will give rise to the emission of Bremsstrahlung. Figure 9 shows a simulated radio image in free-free emission for the case of $v_{\text{XRB}} = 300 \text{ km s}^{-1}$. The emission is edge-brightened, given that it comes exclusively from the compressed ISM shell.

The temperature at the shell of the bubble can be calculated by the post-shock density and pressure as

$$T_{\text{bub}} = \frac{\mu P_1}{k \rho_1} \approx \frac{27}{400} C_1^{2/5} \frac{\mu}{k} \rho_0^{-2/5} L^{2/5} t^{-4/5},$$

where μ is mean molecular mass. If we assume fully ionized gas inside the shell, the free-free surface brightness through the shock can be approximately written as

$$I_{\text{ff}} \approx 3.91 \times 10^{-20} \text{ ergs s}^{-1} \text{ cm}^{-2} \text{ Hz}^{-1} \text{ str}^{-1} \times (\rho_{0H})^2 \left(\frac{t}{1 \text{ Myr}} \right) \quad (31)$$

where we assume a strong shock with $\rho_{\text{shock}} \approx 4\rho_0$ for simplicity.

Free-free emission is dimmer than the synchrotron emission in the bubble, and is expected to be undetectable or marginally detectable at $\nu=1\text{GHz}$.

For the shock temperatures in our simulations ($10^4 - 10^6$ K), optical emission is dominated by cooling lines rather than free-free continuum emission. However, for a fast source the temperature in the bow shock may initially exceed 10^6 K, in which case free-free emission would be the dominant coolant.

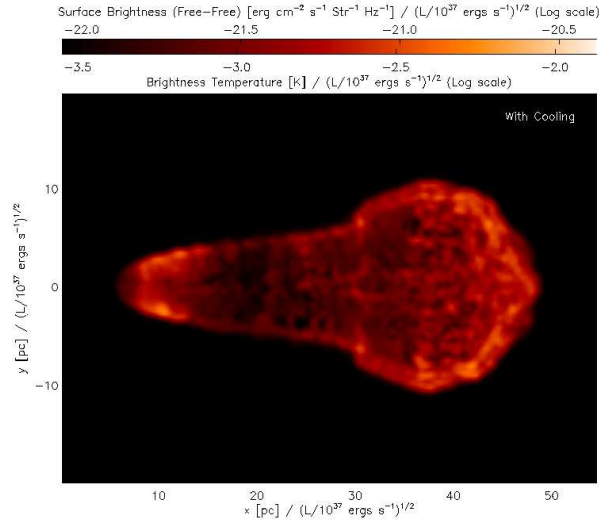


Fig. 9.— Surface brightness of free-free emission for the frequency of 1GHz at 100,000 yr ($v_{xrb} = 300 \text{ km s}^{-1}$).

3.3.4. X-ray

For large enough space velocities, the temperatures at the stagnation point of the bow shock can be sufficiently high to produce X-rays. Fig. 10 shows a simulated Chandra X-ray observation produced using the XIM program (Heinz & Brüggen 2009) for the 300 km s^{-1} simulation at a distance of 5 kpc with a 100 ks exposure at 10^6 years.

For the fiducial parameters, there is a significant flux only from the bow shock, which has a temperature of about 2×10^6 K. However, it may be difficult to distinguish this flux from the emission from the XRB. There is a small amount of X-ray emission from the neck, but it is only marginally distinguishable from the background, and fades as you go farther down the neck.

At early times, the expanding bubble produces a detectable X-ray flux. Figure 11 shows a simulated Chandra X-ray observation for the 300 km s^{-1} simulations (hvc) at a distance of 8 kpc with a 100 ks exposure at 30,000 years. Although it has a low surface brightness, the bubble and neck can be seen, in addition to the bright bow shock, in a smoothed image.

A shock will only be detectable in X-rays if its temperature is above about $5 \times 10^5 \text{ K}$, which corresponds to a shock velocity of about 100 km s^{-1} for the parameters in our simulations. Assuming a strong shock, the shock temperature is

$$T_s \sim 6.79 \times 10^3 K \times M_s^2 \times \left(\frac{P_0}{3 \times 10^{-12}} \right) \left(\frac{\rho_0}{1.67 \times 10^{-24}} \right) \quad (32)$$

The bubble expansion falls below about 100 km s^{-1} at about 36,000 years. After this, the bow shock is still visible, if the XRB is moving fast enough, but the bubble and neck are unlikely to be detected. The bow shock is always visible, but only for XRBs moving faster than about 100 km s^{-1} .

The synchrotron emission from relativistic particles does not produce a detectable X-ray flux.

4. Comparison with SAX J1712.6-3739

While the numerical results and the analytic approximations derived from them are primarily predictive, we can, at the very least, directly apply them through comparisons to the one known XRB with a bow shock nebula.

SAX J1712.6-3739 is so far the only XRB found to display a prominent H_α bow shock nebula (Wiersema et al. 2009). Following the original discovery of the bow shock, a deep VLT observation of the source was obtained to confirm the detection and look for further structure in the H-alpha map. This observation is shown in Fig. 12.

4.1. Data reduction

The data were taken using the Focal Reducer and low dispersion spectrograph (FORS2) on the Very Large Telescope (VLT, Chile), using the $\text{H}_\alpha + 83$ interference filter. As part of a larger programme (ESO programme ID 385.D-0100, PI Russell), we obtained 34 exposures of 60 seconds each on 16 April 2009, under excellent seeing conditions (average 0.7 arcseconds).

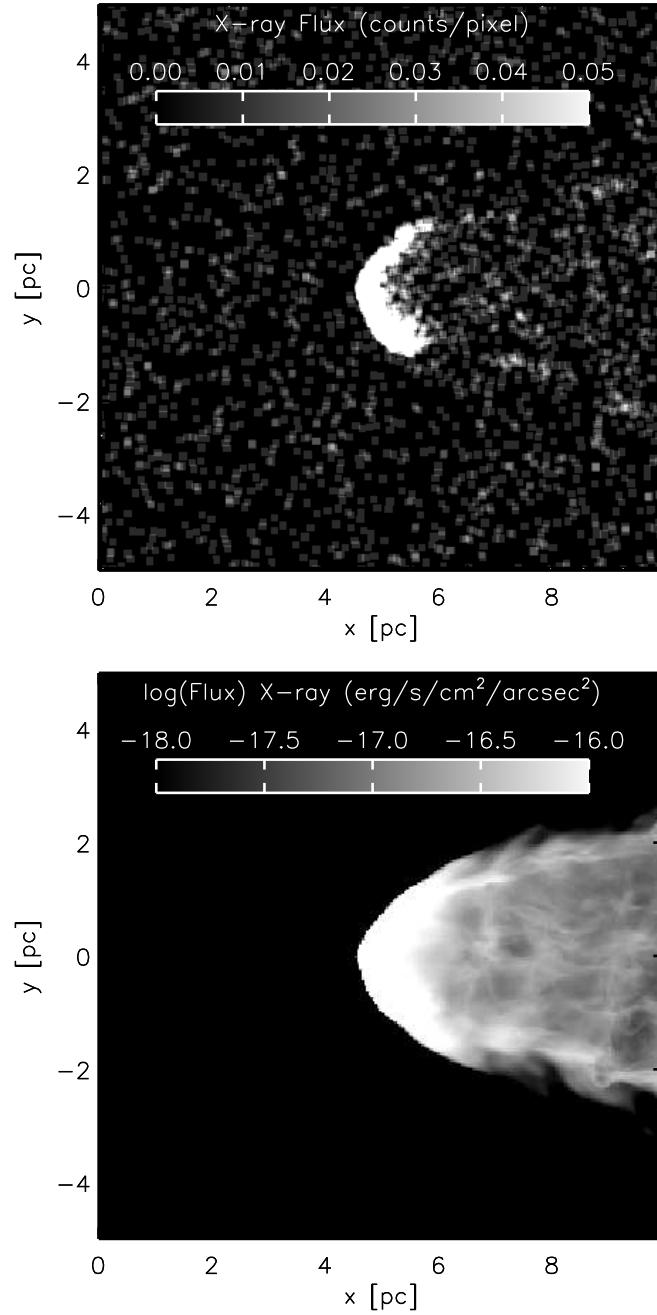


Fig. 10.— Simulated Chandra X-ray image (top) and surface brightness (bottom) of the bow shock for the 300 km s^{-1} simulation at 1 Myr. 100 ks exposure at 5 kpc and flux is integrated from 0.3 to 3 keV. The maximum flux in the bow shock is about 1 count/pixel.

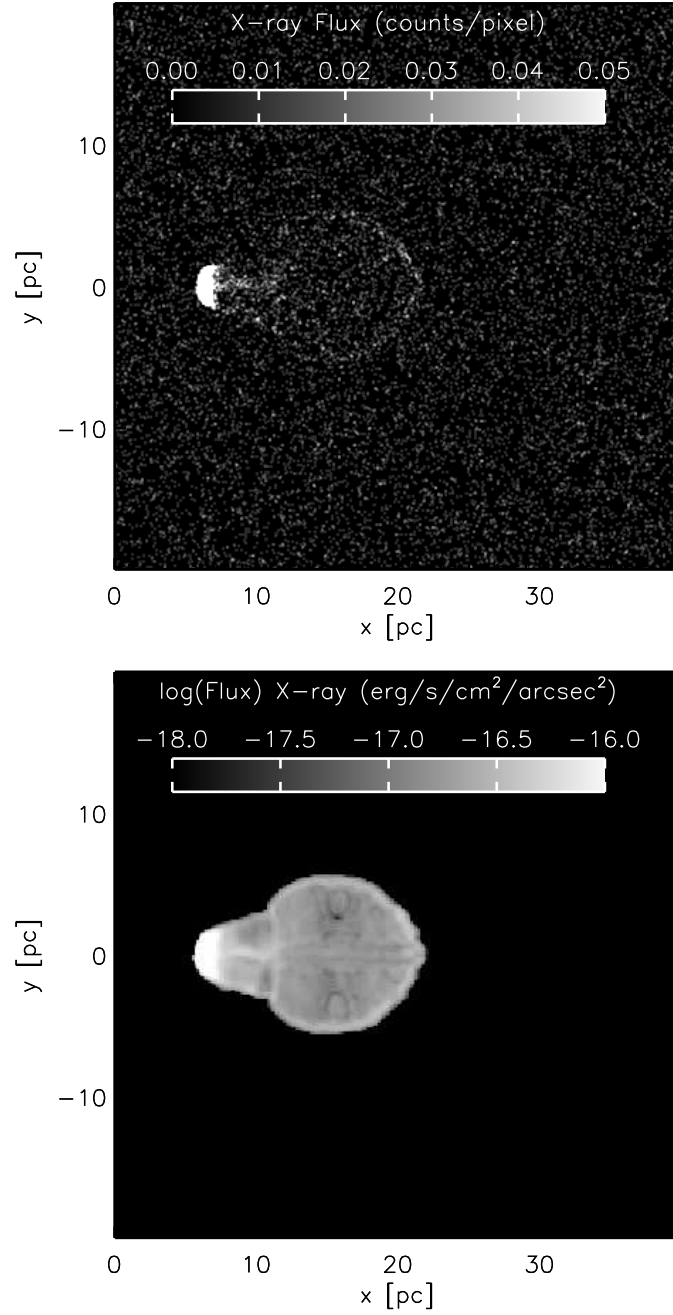


Fig. 11.— Simulated Chandra X-ray image (top) and surface brightness (bottom) of the bubble for the 300 km s⁻¹ simulation (hvc) at 30,000 years. 100 ks exposure at 8 kpc and flux is integrated from 0.3 to 3 keV.

The data were reduced using standard procedures in *IRAF* and combined. Details on the reduction and flux calibration of these data will be reported in a forthcoming publication (Russell et al. in prep.). The FORS2 data cover a much larger sky area than the EFOSC2 data reported in Wiersema et al. (2009) at a better resolution, and have significantly better signal to noise, allowing us to search for fainter features and both small and large scale structure.

4.2. Model comparison

The new VLT observation confirms the presence of a bright bow shock nebula, as first reported in Wiersema et al. (2009). In addition, the image suggests the presence of a roughly circular shell of H_α emission with a radius of $76''$ which connects to the previously observed linear H_α features near the XRB. While the level of patchy background H_α emission makes a firm identification difficult, we interpret this cavity or shell as the bubble inflated by the backflow through the channel. The estimated location of the bubble and neck are sketched in the lower panel of figure 12. The distance from the end of the neck to the center of the bubble is about $190''$.

We estimate the half opening angle of the bow shock seen in the H_α emission to be about 15° , which can be converted into the projected oblique shock angle of $\beta = 0.261799$. From the observed ratio of bubble size to neck length, our analytic model would predict a neck opening angle of about 19° , somewhat larger than the observed value. Assuming the bubble is expanding supersonically, we can set a lower limit on the Mach number of the source from eqn. 19 of

$$M_s \geq \frac{1 + \beta}{\beta} M_b \geq 4.8 \quad (33)$$

For our assumed sound speed of 17.3 km s^{-1} , this implies the velocity of the source is $v_s \geq 83 \text{ km s}^{-1}$. The source could also have a component of motion towards or away from us which is not constrained by the opening angle of the neck.

Given the distance of the object of $D \sim 7 \text{ kpc}$ and the approximate angular size of the putative shell of $76''$, we estimate the physical radius of the bubble to be $R_{\text{bubble}} \sim 2.6 \text{ pc}$. In order to check the consistency between the observation and our model, we carried out a simulation with $v_s = 100 \text{ km s}^{-1}$. Using the scaling relation of bubble radius from eqn. (2) and a standard ISM density of 1 cm^{-3} , the appropriate luminosity is $L = 8.5 \times 10^{33} \text{ ergs s}^{-1}$

and the age of the bubble would be approximately 70,000 years:

$$t_{SAX} \approx 70,000 \text{ yr} \left(\frac{L_{8.5e33}}{\rho_{0H}} \right)^{-1/3} \left(\frac{R_b}{2.57 \text{ pc}} \right)^{5/3} \quad (34)$$

where $L_{8.5e33} = \frac{L}{8.5 \times 10^{33} \text{ ergs s}^{-1}}$.

In terms of source power and ISM density, the velocity of SAX J1712.6-3739 can be estimated to be

$$v_s = 100 \text{ km s}^{-1} \left(\frac{L_{8.5e33}}{\rho_{0H}} \right)^{-1/3} \quad (35)$$

A higher energy (or lower ambient density) implies a higher velocity required of the source by eqn. 35 to have the same neck length at a given bubble size. If the motion of the binary is not perpendicular to our line of sight, but rather inclined at an angle α , then the true opening angle of the source is $\beta_{true} = \beta \sin \alpha$ and the velocity of SAX J1712.6-3739 would have to increase by $1/\sin \alpha$. Eqn. 35 is therefore a lower limit on the source velocity for a given set of parameters. Based on the velocity analysis, a proper motion of SAX J1712.6-3739 can be estimated as a few mas/yr. This proper motion scale will be observable from the LSST. If the velocity is measured directly, it would help to constrain our models and allow us to determine the jet power in terms of just the ambient density or vice versa.

In figure 12, the H_α emission in the neck is brighter than that in the expanding bubble while we expect it to be relatively dim from our fiducial simulations.

It is possible that this is due to the inclination angle for the moving XRBs with respect to the line of sight. If the source is moving at a substantial angle with respect to the plane of the sky, then the amount of neck material we are looking through increases while the thickness of the spherical bubble stays the same. As a result, with some large inclination angle, the emission of the neck can be brighter than that of the bubble.

It is also possible that radiative cooling in the shell around the bubble has moved much of the gas to temperatures too low to emit in H_α , while the neck is still at a sufficiently high temperature to emit, given that the bow shock and Mach cone have a higher Mach number and pressure than the bubble and shell. Because radiative cooling breaks the scale invariance of our simulations, a more detailed investigation would require the construction of a large grid of simulations at different source powers and ISM temperatures, which would be well beyond the scope of this paper.

It is also possible that the relative brightness is simply a result of the complicated morphology of background emission surrounding the observed H_α nebula. The surrounding

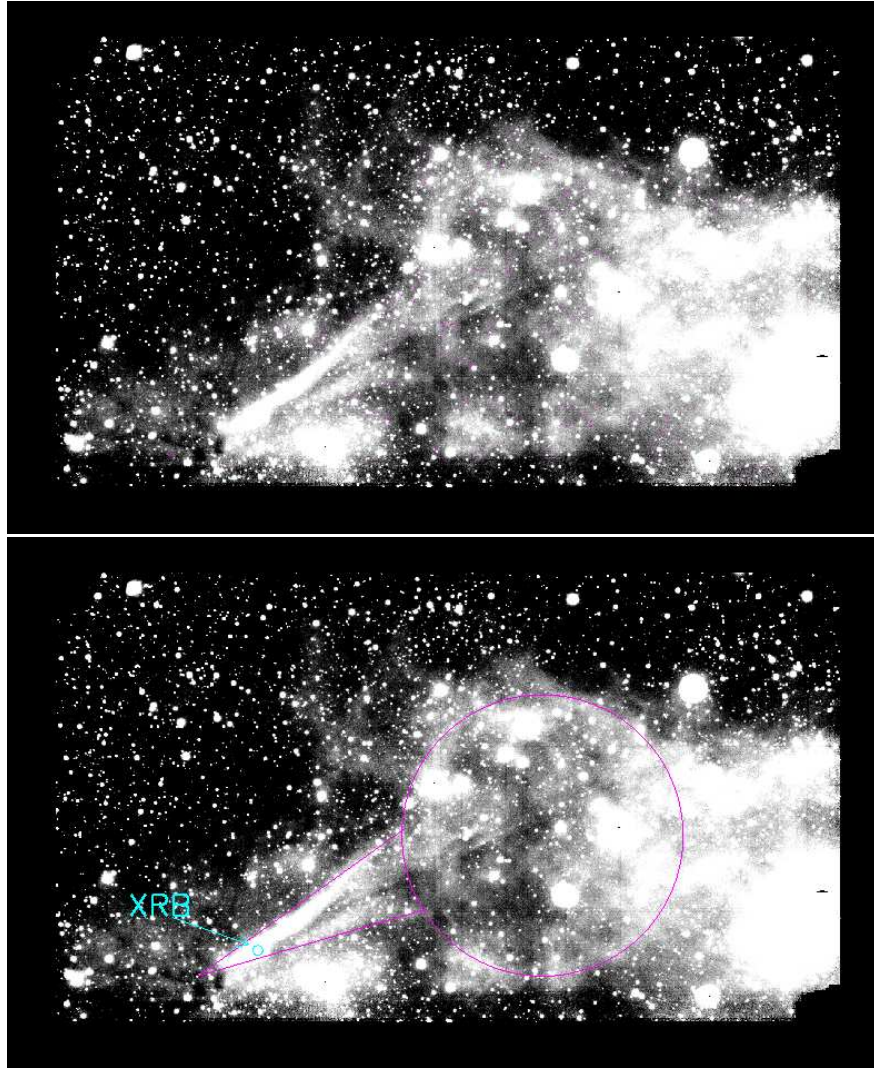


Fig. 12.— SAX J1712.6-3739 image from the VLT FORS2 H_α data (upper panel), and same image with location of the neck and bubble highlighted (lower panel).

emission is clearly non-uniform. A more detailed and quantitative investigation of the new VLT observations is forthcoming in a separate paper.

The difficulty in interpreting the complex structure of the observation notwithstanding, we carried out three simulations with the initial conditions expected to produce a size and shape close to SAX J1712.6-3739 to test whether we could match the observed shape and relative brightness of the neck and bubble. The parameters of these simulations are listed in table 1 as fit1, fit2 and fit3. In figure 13, the top panel shows the results when the ejected energy is $8.47 \times 10^{33} \text{ergs s}^{-1}$ and the velocity of the XRB is 100 km s^{-1} (model fit1). There is bright H_α emission in the bow shock and dimmer but still bright emission from the bubble. However, the emission in most of the neck is relatively dim compared to the shell.

In order to inspect the inclination angle effect, we ran simulation fit2 with a higher velocity of 200 km s^{-1} and display it with an inclination angle of 60° (middle panel). In this case the emission is brightest in the bow shock, part of the neck and the leading edge of the bubble, with somewhat dimmer emission from the trailing edge of the bubble. This is somewhat closer to the bright neck seen in SAX J1712.6-3739, although the location of bright neck emission does not match the observation exactly. The width of the neck relative to the bubble size is about the same as the 100 km s^{-1} case, and there is still a large gap in the neck with very little emission.

Finally, we ran simulation fit3 with a larger power of $L = 2.29 \times 10^{35} \text{ergs s}^{-1}$, and higher velocity velocity of $v_{\text{XRB}} = 300 \text{ km s}^{-1}$ (bottom panel). For the given bubble size, the age is reduced to 23,000 years (eqn. 34). Note that because the emission is significantly brighter in this model, the intensity scale for the bottom panel is increased by a factor of 10 compared to the other two panels to avoid color saturation. In this case, there is no emission from the bow shock, due to the high temperature caused by the faster source. There is bright emission in part of the neck, where the shock has become cool enough to emit in H_α , and there is about equally bright emission from the bubble edges. By varying the source velocity, it is possible to move the location of bright neck emission from the bow shock (for model fit1) far down stream in the neck (for model fit3) and it could be moved even farther away from the XRB for a faster source velocity.

These three simulations differ substantially in their relative surface brightness distributions of H_α emission in bow shock, neck, and shell, showing that it should be possible to construct a reasonable fit to the observations with sufficient fine tuning.

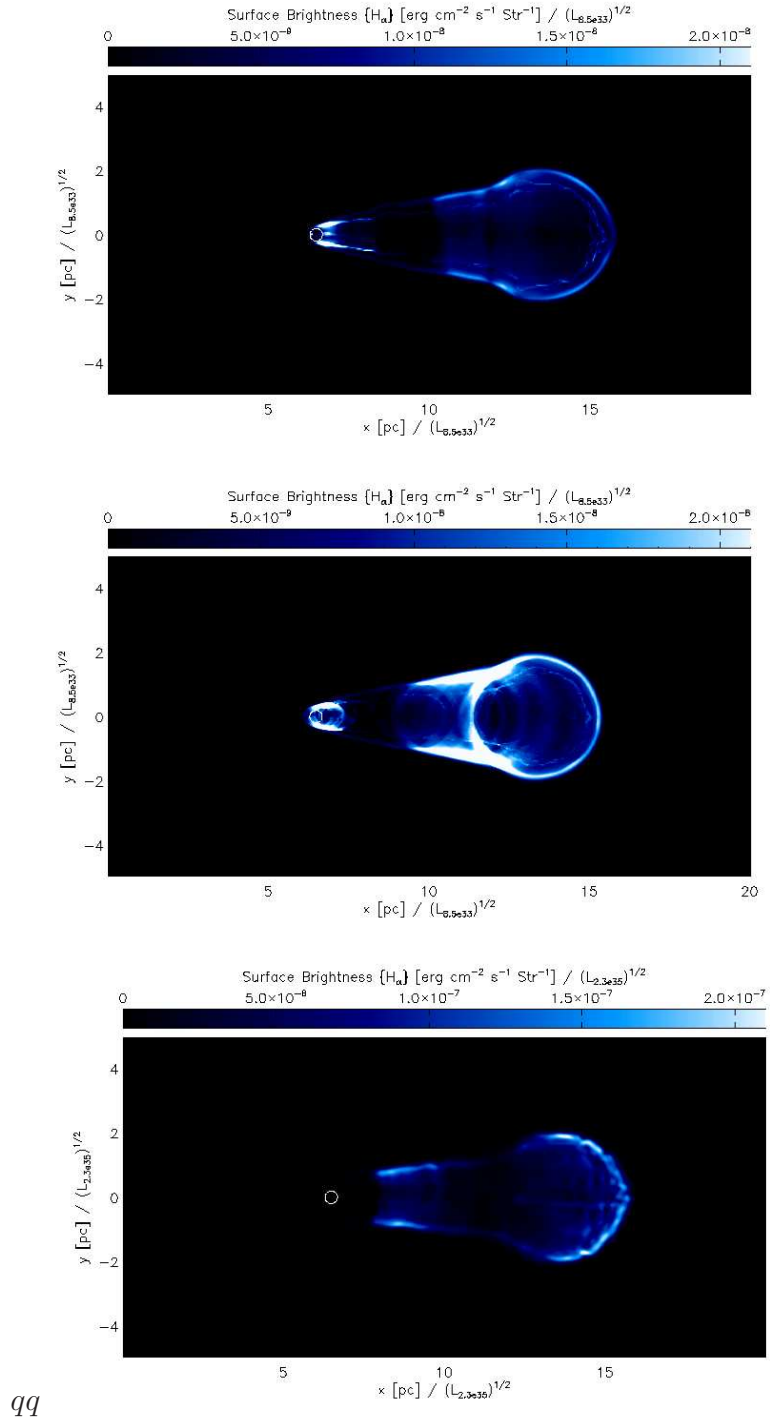


Fig. 13.— H_α images with different initial conditions; $L = 8.47 \times 10^{33} \text{ ergs s}^{-1}$, $v_{\text{XRB}} = 100 \text{ km s}^{-1}$ and edge-on at 69,000 yr (top panel), $L = 8.47 \times 10^{33} \text{ ergs s}^{-1}$, $v_{\text{XRB}} = 200 \text{ km s}^{-1}$ and inclination angle of 60° at 69,000 yr (middle panel), $L = 2.29 \times 10^{35} \text{ ergs s}^{-1}$, $v_{\text{XRB}} = 300 \text{ km s}^{-1}$ and edge-on at 23,000 yr (bottom panel). Note that the intensity scale of the bottom panel is 10 times higher than the other two panels.

5. Conclusion & Summary

By way of numerical simulations, we study the morphological evolution and dynamics of microquasars with high space velocity, the functional equivalent of narrow-angle tail radio galaxies for accreting stellar mass black holes and neutron stars. Such dynamic X-ray binaries initially create a powered, spherically expanding shock/bubble, the expansion of which eventually decelerates to less than the velocity of the XRB relative to the ISM.

When the source reaches the edge of the bubble, it establishes a well defined structure with a bow shock around the source at one end, a spherical bubble at the other, and a neck connecting the bow shock and bubble. The shock angle around neck, β , decreases as the binary moves away from the bubble, but it cannot be less than $1/M_0$, where M_0 is the Mach number of the binary relative to the surrounding medium.

The shocks from all three components creates H_α emission that should be detectable in narrow band imaging. At early times, less than about 30,000 years in our simulations, X-ray emission will be detectable around the bubble and neck, but this rapidly fades as the shock temperature decreases. At later times, X-ray emission is only detectable from the bow shock and only for fast sources ($v_s \geq 100 \text{ km s}^{-1}$).

Synchrotron radio emission from the bubble is bright and covers a large area, but emission from the neck is significantly weaker. There is also strong synchrotron emission from near the binary, but it only covers a small area and thus would be difficult to detect without high resolution. Bubbles created by galactic XRBs should be visible in surveys of diffuse continuum emission. Binaries in other galaxies may also be detectable with a resolution such that the beam size is approximately the size of the bubble. The free-free emission is dimmer than the synchrotron emission and is generally not detectable.

New H_α observations of SAX J1712.6-3739 presented here (see §4) show both a strong bow shock and tentative evidence for a spherical shell trailing the XRB, consistent with the neck and bubble morphology predicted by our simulations. We are also able to constrain the Mach number of the XRB relative to the background ISM to be $M_s \geq 4.8$, corresponding to a velocity of $v_s \geq 83 \text{ km s}^{-1}$ in the plane of the sky for a sound speed of 17.3 km s^{-1} .

Extending our results into pulsar bow shock nebulae (PWBN) is plausible, since bow shock structures of PWBN are well described by the simulations presented in this paper. For example, the H_α images of PSR B2224+65 (Chatterjee & Cordes 2002; Cordes et al. 1993), called “Guitar nebula” for its peculiar shape, shows well developed structures of trailing neck and spherical bubble. We will present models specific to PWBN in a future paper.

We thank Hand-Jakob Grimm, Ellen Zweibel, and Brian Gaensler for helpful discussions. S.H. and D.Y. acknowledges support from NASA/Chandra Theory grant TM9-002X. S.H., D.Y., and B.M. acknowledges support through NSF grant AST-0908690. K.W. acknowledge support from STFC. Based in part on observations made with ESO Telescopes at the Paranal Observatory under programme ID 385.D-0100

REFERENCES

- Bell, J. F., Bailes, M., Manchester, R. N., Weisberg, J. M., & Lyne, A. G. 1995, *ApJ*, 440, L81
- Bernstein, J. P., & Hughes, P. A. 2009, *Journal of Computational Physics*, 228, 6212
- Castor, J., McCray, R., & Weaver, R. 1975, *ApJ*, 200, L107
- Chatterjee, S., & Cordes, J. M. 2002, *ApJ*, 575, 407
- Cordes, J. M., Romani, R. W., & Lundgren, S. C. 1993, *Nature*, 362, 133
- Cox, D. P. 2005, *ARA&A*, 43, 337
- Fender, R. P., Belloni, T. M., & Gallo, E. 2004, *MNRAS*, 355, 1105
- Fryxell, B., Olson, K., Ricker, P., Timmes, F. X., Zingale, M., Lamb, D. Q., MacNeice, P., Rosner, R., Truran, J. W., & Tufo, H. 2000, *ApJS*, 131, 273
- Gaensler, B. M., van der Swaluw, E., Camilo, F., Kaspi, V. M., Baganoff, F. K., Yusef-Zadeh, F., & Manchester, R. N. 2004, *ApJ*, 616, 383
- Gallo, E., Fender, R., Kaiser, C., Russell, D., Morganti, R., Oosterloo, T., & Heinz, S. 2005, *Nature*, 436, 819
- Hao, J. F., & Zhang, S. N. 2009, *ApJ*, 702, 1648
- Heinz, S., & Begelman, M. C. 1997, *ApJ*, 490, 653
- Heinz, S., & Brüggen, M. 2009, *ArXiv e-prints*
- Heinz, S., Brüggen, M., Young, A., & Levesque, E. 2006, *MNRAS*, 373, L65
- Heinz, S., Grimm, H. J., Sunyaev, R. A., & Fender, R. P. 2008, *ApJ*, 686, 1145

- in 't Zand, J., Heise, J., Bazzano, A., Cocchi, M., & Smith, M. J. S. 1999, IAU Circ., 7243, 2
- Körding, E., Rupen, M., Knigge, C., Fender, R., Dhawan, V., Templeton, M., & Muxlow, T. 2008, *Science*, 320, 1318
- Migliari, S., & Fender, R. P. 2006, *MNRAS*, 366, 79
- Miley, G. K., Perola, G. C., van der Kruit, P. C., & van der Laan, H. 1972, *Nature*, 237, 269
- Mirabel, I. F., Dhawan, V., Mignani, R. P., Rodrigues, I., & Guglielmetti, F. 2001, *Nature*, 413, 139
- Rafferty, D. A., McNamara, B. R., Nulsen, P. E. J., & Wise, M. W. 2006, *ApJ*, 652, 216
- Stappers, B. W., Gaensler, B. M., Kaspi, V. M., van der Klis, M., & Lewin, W. H. G. 2003, *Science*, 299, 1372
- Stappers, B. W., Jones, D. H., & Gaensler, B. M. 2002, in *Astronomical Society of the Pacific Conference Series*, Vol. 271, *Neutron Stars in Supernova Remnants*, ed. P. O. Slane & B. M. Gaensler, 141–+
- Sutherland, R. S., & Dopita, M. A. 1993, *ApJS*, 88, 253
- Tudose, V., Fender, R. P., Linares, M., Maitra, D., & van der Klis, M. 2009, *MNRAS*, 400, 2111
- Wiersema, K., Russell, D. M., Degenaar, N., Klein-Wolt, M., Wijnands, R., Heinz, S., Read, A. M., Saxton, R. D., & Tanvir, N. R. 2009, *MNRAS*, 397, L6